A Novel Symmetry-breaking Phase in Two-dimensional FeTe$_2$ with Ferromagnetism Beyond Room-temperature

Liang Liu[1,2], Songsong Chen[1], Zezhou Lin[1], and Xi Zhang[1]*

1. Institute of Nanosurface Science and Engineering, Guangdong Provincial Key Laboratory of Micro/Nano Optomechatronics Engineering, Shenzhen University, Shenzhen 518060, China

2. Key Laboratory of Optoelectronic Devices and Systems of Ministry of Education and Guangdong Province, College of Optoelectronic Engineering, Shenzhen University, Shenzhen, 518060

Corresponding Author

*e-mail address: zh0005xi@szu.edu.cn

Abstract

Recently, ferromagnetism observed in monolayer 2D materials draws attentions due to the promising applications in next-generation spintronics. Here, we predicted a novel symmetry-breaking phase in 2D $FeTe_2$ which differs from conventional transition metal ditellurides shows superior stability and room-temperature ferromagnetism. Through DFT calculations, we found the exchange interactions in $FeTe_2$ consist of short-range super-exchange and long-range oscillatory exchanges mediated by itinerant electrons. Up to 6 nearest neighbor (NN), the exchange constants are calculated to be 50.95meV, 33.41meV, 2.70meV, 11.02meV, 14.46meV and -4.12meV, respectively. Furthermore, the strong relativistic effects on Te^{2+} induce giant out-of-plane exchange anisotropy and open up a significantly large spin-wave gap of Δ^{SW}=1.22meV. All these lead to the robust ferromagnetism with Tc surpassing 423K, which is predicted by renormalization group Monte Carlo method, sufficiently higher than room-temperature. The findings herewith shed a light for the promising future of $FeTe_2$ in 2D magnetic researches and spintronic applications.

TOC GRAPHICS
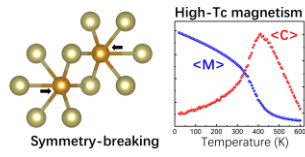
The novel symmetry-breaking phase and high-Tc ferromagnetism in FeTe$_2$

Since the discovery of two-dimensional (2D) van der Waals crystals, 2D materials have attracted extensive attentions due to their excellent physical properties. Constant research has been conducted to explore the magnetic properties of 2D materials. As the core of many theories,[1-3] the two-dimensional magnetism promotes the study of topology, the spin wave,[4] experimental and technological generation of new phases and spintronics.[5-6] Due to its superior strain, chemical, optical and electrical properties,[6-9] 2D magnetism are expected to have a wide range of applications in future 2D heterostructures.[10] Therefore, there is a lot of work dedicated to explore magnetism in two-dimensional materials e.g., defect and doping engineering,[11-15] edge quantum well[16-20] and epitaxial growth of magnetic thin films. Recently, the intrinsic magnetism was also observed in mechanically exfoliated and atomic thin CrI_3 and $Cr_2Ge_2Te_6$ van der Waals (vdW) crystals by polar magneto-optical Kerr effect.[21-22] The quasi-free-standing structures of these vdW magnets provide excellent flexibilities to integrate with other devices to realize muti-functional applications.[23-32]

Nevertheless, most of the observed 2D magnetic orders can only persist under ultra-low temperatures as a consequence of Mermin-Wagner theorem,[33-38] which demonstrates that isotropic and short-coupled 2D ferromagnetism is easily destroyed by thermal fluctuations.[21, 39] To date, 2D ferromagnetism beyond room-temperature was only observed in limited systems. VSe_2 is the first observed room-temperature 2D magnetic system, which is still in debate since VSe_2 has in-plane continual anisotropy indicating no long-range orders corresponding to the analytical theory. As well as, X-ray magnetic circular dichroism measurements found no intrinsic magnetic signals in VSe_2, suggesting the role of substrates.[40-42] The room-temperature ferromagnetism was also observed in $MnSe_2$,[43] which shows no anisotropy or small depend on the substrate. On the other hand, the theoretical investigations based on first-principle

calculations play essential roles in the research of 2D magnetism via providing promising candidates and deep mechanism.[44-45] Very recently, C. Huang *et. al* reported a systematic method to enhance the coupling strengths based on an elaborate double-orbital model[46], and several 2D magnetic systems with ultra-high Tc were then predicted by first-principle calculations.[47-49]

In this work, we predicted a novel symmetry-breaking phase in $FeTe_2$ with robust ferromagnetism far beyond room-temperature. First-principles calculations are performed to study the electronic and magnetic properties of $FeTe_2$. We observed the spontaneous symmetry-breaking in $FeTe_2$ which is more stable and completely distinct from conventional transition metal ditellurides (TMDs). In the new phase, exchange interactions consist of ferromagnetic super-exchange and long-range oscillatory exchange mediated by itinerant electrons. We considered exchange constants up to 6 nearest neighbouring (6NN) and their strengths are 50.95 meV, 33.41 meV, 2.70 meV, 11.02 meV, 14.46 meV and -4.12 meV, respectively. Furthermore, relativistic calculations showed that the out-of-plane magnetic anisotropy inherent in $FeTe_2$ layers reaches ~3meV/u.c., which is a significantly large value in record. The long-range ferromagnetic orders in ground states are verified by the anisotropic spin-wave theory. And the phase transition is studied via renormalization group Monte Carlo method, which predicts the Curie temperature of $FeTe_2$ is as high as 423 K. All these indicate that the novel symmetry-breaking phase in 2D $FeTe_2$ is an excellent candidate to realize room-temperature 2D ferromagnetism and will surely merit future spintronic applications.

The three possible geometry structures of the two-dimensional $FeTe_2$ are shown in Fig. 1a, including the two symmetric phases i.e. T-phase and H-phase with C_{3v} symmetry and the symmetry-breaking phase with C_{2h} symmetry, which is similar to the T'-phase in MoS_2. Firstly, let us consider the two symmetric phases. As shown in Fig. 1c, vibration modes with large

negative frequencies were presented in T-phase, signifying the structural instability, while the negative frequencies in H-phase are negligible. These are in agreement with previous studies and may be the reason why previous theoretical investigations on FeTe$_2$ were all focused on H-phase[50-52]. However, the previous studies only considered the low-spin state of T-phase, and the high-spin state was neglected.[51] As shown in Fig. 1b, we found low-spin (2.38μB per Fe ion) and high-spin states (2.81μB per Fe ion) in T-phase FeTe$_2$, and the later one was energetically favored than H-phase, indicating that H-phase is also metastable, too. The total energies of 1T and 2H phases are obtained as E= -12.81eV (1T low-spin phase), -12.90eV (1T high-spin phase), and -12.83 (2H phase) respectively. The energies of 1T and 2H phases are both higher than the E=-12.95eV of symmetric breaking C$_{2h}$ phase, indicating that the C$_{2h}$ phase is the most favorable. Fig. 1b also shows the energy of structures between symmetric C$_{3v}$ T-phase and C$_{2h}$ phase. The landscape describes the energy evolution with the superposition of two structures of 1T-high spin phase and symmetric breaking C$_{2h}$ phase. These middle structures were constructed by linear mixing of two ends. α is the superposition coefficient. The energy barrier between the symmetric and symmetry-breaking phase is found to be 139.4 meV. Therefore, one can always obtain the symmetry-breaking phase via heating from the symmetric phase of FeTe$_2$ monolayers.

The stable phase of monolayer FeTe$_2$ can be inferred from the negative-frequency vibration mode in T-phase. As shown in Fig. 1d, the soft mode corresponds to the dimerization of Fe ions and distortion of Te layers, finally leading to the symmetry-breaking phase with symmetry group of C$_{2h}$. This kind of simultaneously symmetry-breaking process can be well understood by the mechanism of Piers-distortion. The symmetry-breaking phase with C$_{2h}$ is similar to the T'-phase in MoS$_2$, but the magnetic state is different. In symmetric T-phase, Fe ions were far from Te and

bonding states cannot be formed effectively. Biasing from the center shortened Fe-Te distance, thus is favored for bonding.

Table 1 lists the optimized lattice parameters for the symmetry-breaking C_{2h} phase, and this structure was demonstrated to be kinetically stable by the phonon spectra. As shown in Fig. 1c, only negligible negative frequencies around the Γ point were presented, which may be ascribe to the inaccuracies in the calculation of Hessian matrix. Even if the soft modes were true, they correspond to the long-wave vibrating modes such as cripples in large samples (with length > 100 nm). For small samples, these soft modes were inactive due to the confinement. Fig. 1d shows the soft mode in C_{2h}, in which every atom vibrates in the same direction, causing no distortions.
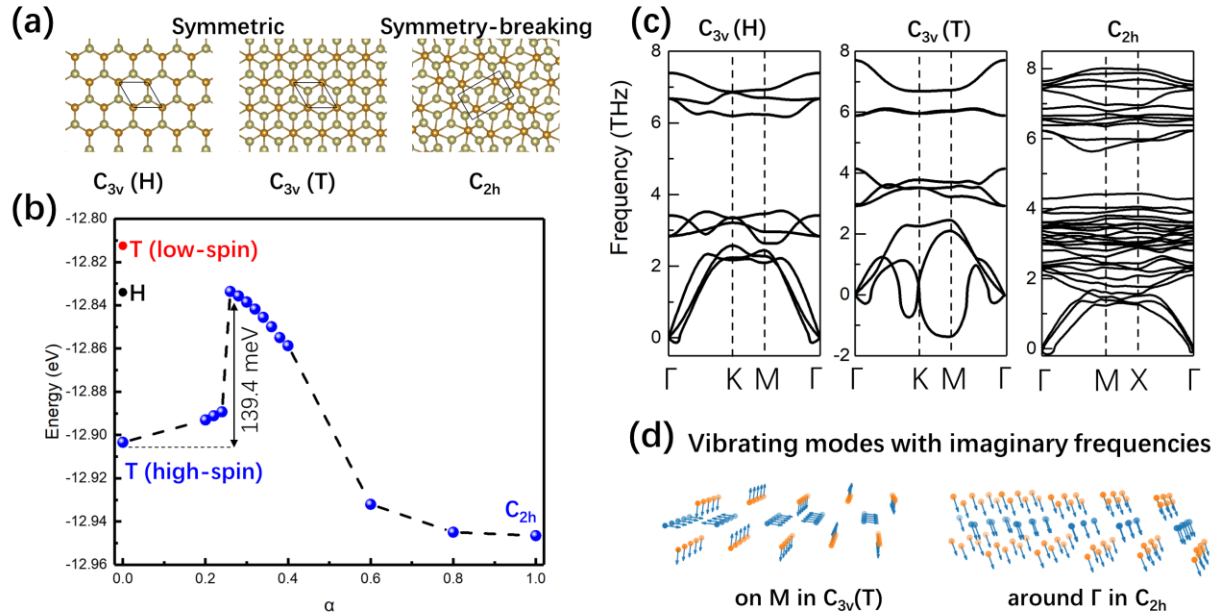
Figure 1. Topview of (a) two symmetric and one symmetry-breaking geometry structures for optimized 2D FeTe$_2$. Balls with light and deep colors correspond to the Fe and Te ions. Black lines denote the border of unit cell. (b) The total DFT energies for T-phase with low-spin (red dot), H-phase (black dot),

T-phase with high-spin (blue dot in left), symmetry-breaking phase (blue dot in right) and the structures between T (high-spin) and symmetry-breaking phases (blue dots). The horizontal coordinate α for each mediating structure corresponds to the linear mixing factor. (c) Phonon spectra for symmetric H- and T-phase and symmetry-breaking C_{2h} phase. (d) The vibrating modes correspond to the lowest state at M-point for symmetric T-phase and the lowest state near Γ-point for symmetry-breaking phase, respectively. Blue and orange dots correspond to the Fe and Te ions and arrows denote the vibrating directions.

Table 1. The lattice parameter a, b, the horizontal biased distance δh and vertical biased distance δv of Fe ions from the centre of hexagonal Te-framework.

a (Å)	b (Å)	δ_h(Å)	δ_v(Å)
5.884	3.529	0.351	0.130

The spin-polarized calculations manifested that the ground state of $FeTe_2$ is spin-polarized and one unit-cell involving two Fe ions possesses $4\mu B$ magnetic moment. The local magnetic moment on Fe ion is $\sim2.4\mu B$, larger than the mean-value $2\mu B$, which is induced by the super-exchange process and we would discuss later. Fig. 2a shows the band structure of the FM structures in which the conduction bands and the valence bands are interlaced, indicating that $FeTe_2$ exhibits metallic properties and itinerant magnetism in which the exchange interactions between local magnetic moments can be very long-range with the help of itinerant messengers.
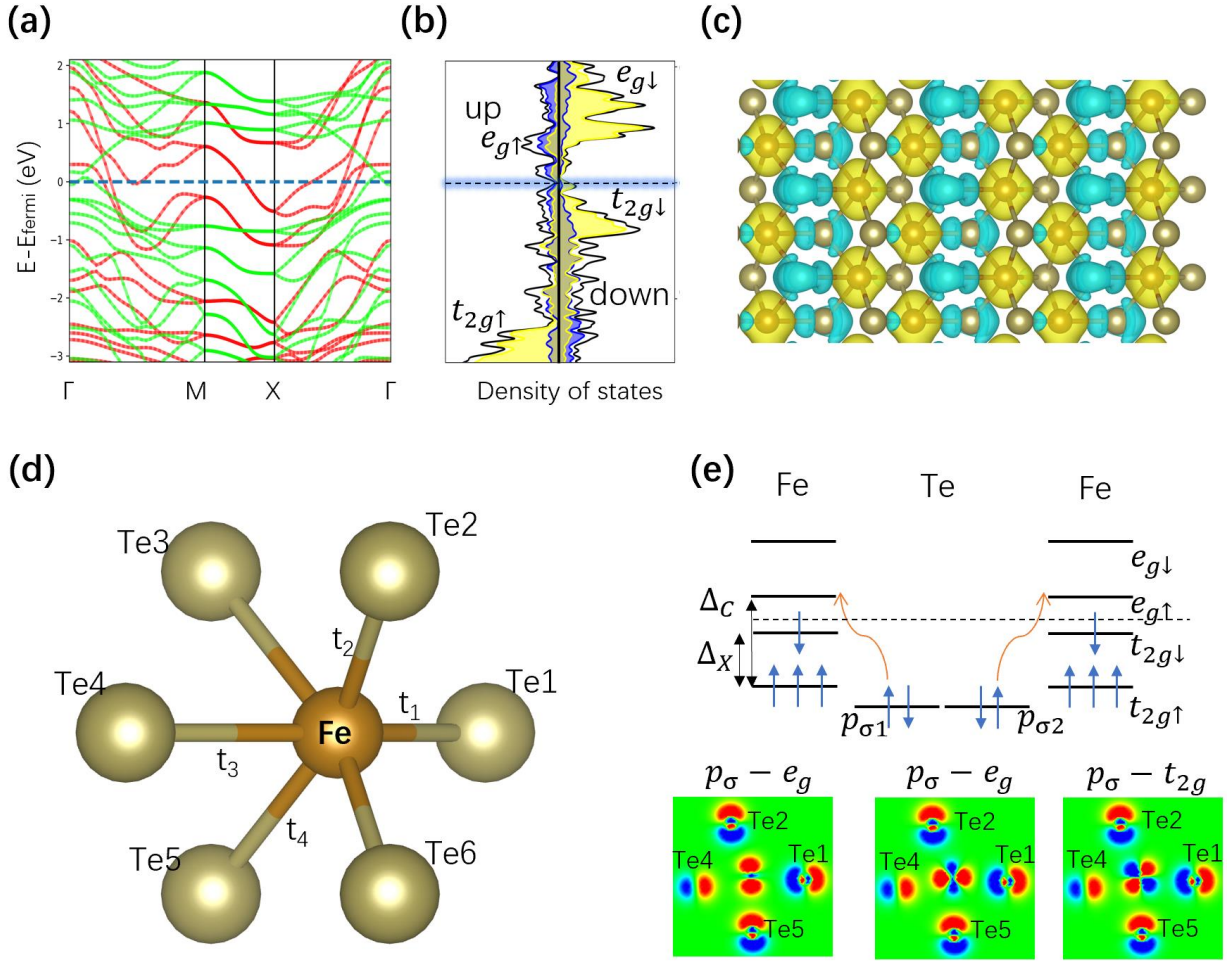
Figure 2. (a) Band structure with Fermi energy fixing to zero. Up- and down-spin channels are denoted by red and green lines. (b) PDOS. (c) Spin density isosurface with surface level equal to 0.004 electrons/$Å^3$. Positive and negative density are colored with yellow and blue, corresponding to the up- and down-spin channels, respectively. (d) Distorted Fe-Te octahedra. Four representative p-d hopping are denoted by $t_1 \sim t_4$. (e) Up panel: principal p-d hopping between Fe and Te ions. Solid lines denote the energy levels and small arrows denote occupations of spins. Horizontal dashed line represents Fermi level and curved long arrows correspond to the path of principle p-d hopping. Down panel: atomic wavefunctions projected to the plane expanded by Te_1, Te_3 and Te_5. Only p_σ orbitals were given for Te, and d_{x2-y2}, d_{z2}, d_{xz} orbitals were given for Fe, respectively.

To further understand the magnetism in FeTe$_2$, the projected density of states (PDOS) is plotted in Fig. 2b. One can see that the exchange splitting in d-shell Δ_X is slightly smaller than the crystal field splitting Δ_C, mediating the low-spin states in the Fe-d shell. In addition, the strong electron-electron interactions in d-shell split the spin-down t$_{2g}$ orbitals into upper and lower Hubbard bands, and the occupied d-states were nearly gapped from empty d-states, mediating the integer nature of magnetic moment.

We also plot the isosurface spin density in Fig. 2c to visualize the real-space distribution of net spin. It is evident that the magnetism is mainly contributed by the Fe atoms, which is consistent with the results obtained from PDOS. Furthermore, non-negligible polarized spin density on Te ions is also presented, and the real-space distribution is significantly anisotropic, which can be also ascribed to the super-exchange in distorted octahedra as discussed below.

We describe the electronic structure in FeTe$_2$ by a simple tight-bonding model:

$$H = \sum_{i\alpha\sigma} \varepsilon_{i\alpha\sigma} c_{i\alpha\sigma}^{\dagger} c_{i\alpha\sigma} + J_{xy} \sum_{i,\alpha\neq\beta} S_{i\alpha} S_{i\beta} + \sum_{i\neq j\alpha\beta\sigma} t_{i\alpha j\beta} c_{i\alpha\sigma}^{\dagger} c_{j\beta\sigma} \qquad (1)$$

where the three terms correspond to the onsite energy, on-shell exchange and hopping process. Up to mean-field approximation (MFA), all the electron-electron interactions e.g., the exchange splitting Δ_X and crystal splitting Δ_C are included in onsite energies as shown in the upper part of Fig. 2e.

Fig. 2d shows the four approximately co-plane hopping tunnel t$_1$~t$_4$, and the lower part of Fig. 2e shows the atomic wavefunctions projected to this plane. Apparently, the hopping processes

are dominated by the p_σ-e_g while p_σ-t_{2g} hopping are nearly forbidden in t_1, t_3, t_4 tunnels due to the symmetry, but available in t_2 tunnel due to the symmetry-breaking caused by distortion. Therefore, up to 1st order perturbation of hopping, the p_σ orbitals in t_1, t_3 and t_4 directions are polarized with spin-down states while the polarization in t_2 directions is much less, in line with the spin density distribution in Fig. 2c. As the exchange, the e_g orbitals in Fe are also partially spin polarized with up-spin, enhancing the magnetic moment on Fe. Furthermore, expanding the hopping process to 4th order, we can obtain the ferromagnetic exchange for 1~3NN Fe ions, i.e. the cation-anion-cation type of super-exchange. And one can see Supporting information for more details.

To further figure out the detail magnetic structures especially the properties of long-range exchange interactions, we employed Heisenberg model:

$$H = -\frac{1}{2}\sum_{ij} J_{ij}S_iS_j - \frac{1}{2}\sum_{ij} B_{ij}S_i^z S_j^z + A\sum_i (S_i^z)^2 \qquad (2)$$

in which S_i represents spin of Fe ion in ith site. J and B represent the isotropic and anisotropic parts of exchange interactions respectively. A represents the single-ion magnetic anisotropy on Fe. We consider the exchange couplings up to 6th nearest neighbors (6NN) and all parameters in eq.2 were solved by energy mapping from relativistic DFT calculations on seven 3x3 supercells including one with ferromagnetic (FM) configuration and six additional systems with nonequal AFM configurations (see Method section for more details about energy mapping from DFT to eq. 2).

Fig. 3b shows the detail magnetic configurations for the six AFM cases, in which the red and blue dots represent the Fe ions with up and down net spins respectively. Two Fe connected by a

solid line have the same spin direction and represent the ferromagnetic bond. In contrast, the two Fe atoms connected by a dashed line have opposite spin directions, which represent an antiferromagnetic bond. The red, green, blue, violet, orange and yellow lines denote the 1 to 6 nearest neighboring between Fe ions, respectively. Fig. 3c represents the anisotropic energy for ferromagnetic system with different spin orientations. In the XZ-panel perpendicular to the 2D atomic plane of $FeTe_2$, the energy with easy magnetic orientation is lower than hard orientation by almost 3 meV, which is a significantly strong value for magnetic anisotropy comparing to known systems[44-45, 53-54]. The magnetic anisotropy in the XY-panel parallel to the 2D atomic plane is also as large as ~1 meV. The ultra-strong anisotropy inherent in $FeTe_2$ can be ascribed to two aspects viz. i) the biasing of Fe ions from the centers of octahedra lifts the O_h symmetry and induced single-ion anisotropy with 2nd order; ii) Te ions embedded in the path of super-exchange provided large contributions of exchange anisotropy since Te were also spin-polarized in the exchange process as we discussed before, and the relativistic effects on Te ions are strong enough to induce significant spin-orbital-coupling.
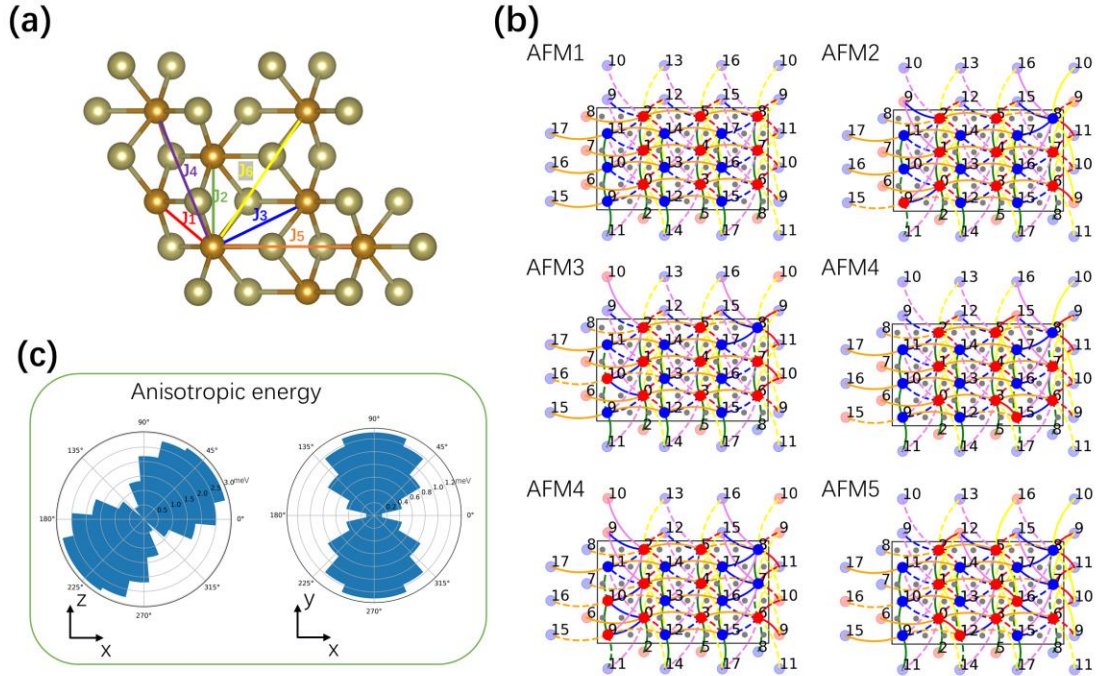
Figure 3. (a) the exchange path for 1 to 6 nearest neighbored Fe pairs (b) the six AFM configurations for FeTe$_2$ utilized in this work. Red and blue dots represent the Fe ions with up and down net spins. Solid and dashed lines denote the FM and AFM type of bonds between Fe, respectively. (c) relative energies for magnetic anisotropy in the XZ-plane (perpendicular to the atomic plane) and YZ-plane (parallel to the atomic plane), respectively.

Table 2 lists all magnetic parameters in Heisenberg model. The exchange interactions (isotropic part) turn out to be: J(1)= 54.08 meV, J(2)= 13.11 meV, J(3)= 6.11 meV, J(4)=2.45 meV, J(5)=33.66 meV and J(6)=-2.93 meV, respectively. The exchange interactions oscillate along with the growing of coupling range and preserve non-negligible strength even at 6NN, indicating the long-range and RKKY-like coupling nature inherent in FeTe$_2$. This can be ascribed to the itinerant electrons which play as messengers, spreading the exchange interactions between two local magnetic moments on Fe ions far apart. In addition, because of the long stretching of 5p-orbitals of Te ions, the super-exchange of cation-anion-anion-cation can

contribute to the long-range coupling nature, too. Most importantly, the single-ion anisotropy A is -1.14 meV, showing out-of-plane preferring. And the anisotropy in exchange interactions B are shown to be giant, revealing the crucial roles of Te ions.

Table 2. Single-ion anisotropy and anisotropic exchange constants up to 6th nearest neighbored for $FeTe_2$.

Range	1NN	2NN	3NN	4NN	5NN	6NN
J (meV)	50.95	33.41	2.70	11.02	14.46	-4.12
B (meV)	0.81	-1.68	0.28	0.55	0.69	1.17

A=-1.14 meV

To figure out the stability of ferromagnetic order, especially for large scales, we calculated the spin-wave spectra based on Heisenberg Hamiltonian (eq. 2) and Holstein-Primakoff transformations. The harmonic part of spin-wave Hamiltonian is:

$$H_0 = -S \sum_{ij} (J_{ij} + B_{ij}) n_i - J_{ij} b_i^\dagger b_j - 2A_z S \sum_i n_i \qquad (3)$$

in which $b_i^\dagger (b_i)$ creates (annihilate) one spin-wave in i[th] site. And the interacting part is:

$$H_1 = \frac{1}{2} \sum_{ij} (J_{ij} + B_{ij}) n_i n_j - J_{ij} b_i^\dagger n_i b_j + A_z \sum_i n_i^2 \qquad (4)$$

Fig. 4a shows the spectra of interaction free spin-wave. No negative eigenvalues can be found amongst the whole Brillouin zone, demonstrating that the FM configuration is kinetically stable in ground state (in ground state, there are no occupations of spin-waves thus no need for the considerations on interactions). Due to the strong anisotropy inherent in the magnetism of $FeTe_2$, the energy gap of spin-wave Δ^{SW} at the Γ point is as high as 1.22 meV, shown in the inset of Fig.

4a, which is also a significantly large value to suppress the thermal excitations[44-45, 48], fulfilling the condition to break out the forbidden of Mermin-Wigner theorem.
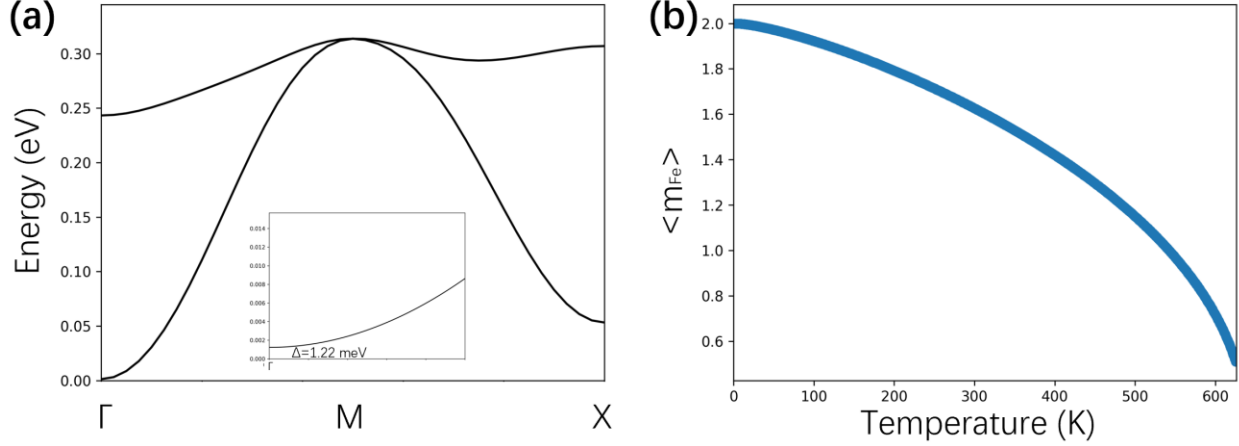
Figure 4. (a) spectra of free spin-wave. Inset shows the spectra near Γ point (b) evolution of remain magnetism with increasing of temperature up to MFA and RPA.

Based on MFA and the random phase approximation (RPA), the remain magnetism can be expressed as:

$$\begin{cases} \langle m \rangle = 2(S - \langle n \rangle) \\ \langle n \rangle = \frac{1}{N} \sum_{k \in BZ} \frac{1}{e^{\beta \tilde{\varepsilon}(k)} - 1} \end{cases} \quad (5)$$

Here $\langle n \rangle$ denotes the averaged occupation number of spin-waves, $\tilde{\varepsilon}(k)$ is the renormalized spin-wave spectra with MFA, $\langle m \rangle$ is the averaged magnetic moment per Fe ion, and N is the supercell size of spin-wave system. Since $\tilde{\varepsilon}(k)$ is relied on the occupation $\langle n \rangle$, equation 3-5 can be solved iteratively. Fig. 4b shows the evolution of remain magnetism up to MFA and RPA. Apparently, the system can sustain finite magnetism even beyond 600K, revealing excellent robustness against thermal fluctuations.

15

To avoid the deficiencies of MFA and RPA near the phase transition, and find out the exact Curie temperature (Tc) in FeTe$_2$, we conducted the Monte Carlo simulations based on the fully anisotropic Heisenberg model. Spins were treated as classical vectors which were allowed to rotate and point to any space orientations. In order to reduce the autocorrelations near the Tc, we implemented the Wolff algorithm on a 32x32 super-lattice.

Fig. 5a shows the evolution of averaged net magnetic moment and specific heat capacity per Fe with increasing of temperature. In low temperature region with T<100K, the magnetism predicted by Monte Carlo simulations were close to the RPA results in Fig. 4b. The maximum of heat capacity is around 400K. To avoid errors origin from the finite size effects, we employed the real-space renormalization group analysis, in which the original 32x32 lattice was coarsely grained into 16x16 lattice with every four neighbored spins forming quasi-particles and the representative spin of each quasi-particle was determined according to the majority rule. And the dynamics (that is, the Heisenberg Hamiltonian) of renormalized model were assumed to be the same as before. Therefore, we can calculate the internal energy of renormalized system with eq. 2, too. In Fig. 5b, the evolution of internal energies of original spin model U(K) and renormalized quasi-particle model Ũ(K) were represented by red and blue dots, respectively. The transformation of renormalization group pushes the two lines of inert energy apart from each other at every temperature but leaves 423K fixed. Therefore, we claim that the phase transition of ferromagnetic orders in FeTe$_2$ occurred at 423K exactly, which is sufficiently higher than room-temperature.
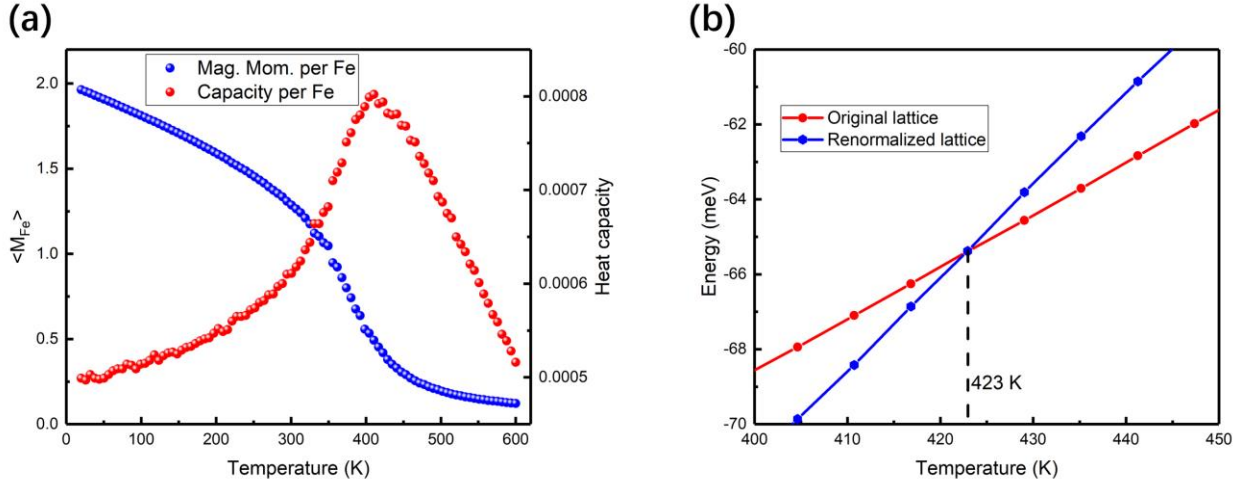
Figure 5. (a) evolution of Monte Carlo averaged spin (blue) and specific heat capacity (red) per Fe. (b) nearly linear evolution of internal energy per unit cell in original 16x16 superlattice of spins (red) and renormalized 32x32 superlattice of quasi-particles (blue), respectively. Lines are guiding eyes.

In summary, using DFT (GGA+U with full considerations on relativistic effects), we have systematically studied the electronic and magnetic properties of 2D $FeTe_2$. The following conclusions can be drawn: (1) We have found that the symmetric H- and T-phase are metastable and T-$FeTe_2$ undergoes spontaneous dimerization and symmetry breaking from C_{3v} to C_{2h}. (2) Prove that the 2D $FeTe_2$ exhibits exciting long-range ferromagnetism, and the out-of-plane magnetic anisotropy found in $FeTe_2$ here is significantly large among know reports. (3) By applying renormalization group Monte Carlo method based on the anisotropic Heisenberg model, we demonstrated that the Curie temperature of the symmetry-breaking $FeTe_2$ is as high as 423 K, far beyond room-temperature. All these provide a novel phase for $FeTe_2$, as well as suggest a promising candidate for future room-temperature applications in spintronics.

17

Computational Method. We calculated the geometric relaxation and electronic structure within Vienna atomic simulation pack (VASP), both based on spin polarization density functional theory (DFT) with full considerations on relativistic effects. Projected augmentation plane wave basis (PAW) is employed with plane waves are truncated at 400 eV. The Perdew-Burke-Ernzerh (PBE) form functional is used for the implementation of generalized gradient approximation (GGA).[55] Periodic boundary conditions applied to the $FeTe_2$ monolayer calculation. A vacuum space perpendicular to the layer is set to 20 Å to prevent the unphysical layer-to-layer interactions between neighboring slabs. Unit cells were used for the energy comparison amongst 1T-, 2H-, symmetry-breaking, and other structures of $FeTe_2$. And 3×3 supercells were used for magnetism calculation. Brillouin zone is sampled with a resolution of $2\pi \times 0.03\text{Å}^{-1}$ using Monkhorst-Pack method[56]. The structural optimization is carried out until the maximum force and displacement converge to 0.001 eV/Å and 0.001 Å, respectively. The self-consistency threshold of total energy was set at 10^{-6} eV/atom.

In DFT calculations, the GGA functional has an admitted disadvantage that it underestimates the strong interactions of d-electrons inherent in transition metal compounds. Previous studies have reported that the standard GGA or LDA functional cannot even converge to the correct magnetic ground states in symmetric H-phase $FeTe_2$, and GGA + Ueff method with Ueff = 2.0 eV for d-electrons of Fe can result in the same magnetism as hybrid exchange-correlation functional (HSE06).[50-51, 57-58] In this work, we also found the similar cases in C_{2h} $FeTe_2$. With bare GGA, DFT converged to nonmagnetic ground state, while GGA + Ueff on Fe-d with 2.0eV led to 4μB magnetic moment which was also indicated by HSE06 functional. Therefore, our DFT calculations for magnetism within supercells were performed with Ueff = 2.0eV for Fe-d shell.

The computation of magnetic constants via energy mapping from DFT to Heisenberg Hamiltonian eq. 2 was done as below. Consider the case in which all spins point to x or y directions, the second and third terms in eq. 2 vanish. Therefore, eq. 2 leads to the following energy expression:

$$E_i^{x(y)} = E_0 + \frac{S^2}{2} \sum_d N_i(d) J_{x(y)}(d) \qquad (6)$$

in which $E_i^{x(y)}$ is the total DFT energy of ith spin configurations with all spins pointing to x(y) direction. $N_i(d) = N_{FM}^i(d) - N_{AFM}^i(d)$ is the number difference between d^{th} nearest neighbored (dNN) FM bonds and AFM bonds. FM bonds are bonds which link two spins with the same direction, and AFM bonds are exactly opposite. Eq. 6 can be uniquely solved with D+1 different spin configurations if the exchange couplings were not longer than D^{th} NN. Meanwhile, the energy expression of z-oriented spin configuration is:

$$E_i^z - E_0 = NA_z S^2 + \frac{S^2}{2} \sum_d N_i(d) J_z(d) \qquad (7)$$

where N is the number of magnetic ions. Since we have already obtained E_0 in eq. 6, this equation can also be uniquely solved using D+1 different magnetic configuration. After some straight algebras, and note that $J(d) = (J_x(d) + J_y(d))/2, B(d) = J_z(d) - J(d)$, we can get all parameters in eq. 2.

The Monte Carlo simulation with Wolff algorithm based on classical Heisenberg model is used to describe the thermal dynamics of magnetism in equilibrium states.[59-61] At each temperature, we start with ferromagnetic configurations and use 40000 sweeps to sufficiently thermalize the system into equilibrium, and all statistical results are obtained from next 320000

sweeps. Specific heat capacity is calculated by dissipation-fluctuation theorem. Real-space renormalization group with majority rule is used to analyze the phase transition and locate the Curie temperature. All the renormalization group Monte Carlo algorithms described here were implemented in our open source project MCSOLVER.[62]

Notes

The authors declare no competing financial interests.

Supporting information available: perturbation theory for the tight-bonding model (eq. 1), expressions for perturbated many-body states (equation S1 and S2), expressions for 4th order super-exchange (equation S3-S5).

REFERENCES

(1)   Kitaev, A. Anyons in an Exactly Solved Model and Beyond. *Ann. Phys.* **2006,** *321*, 2-111.
(2)   Lee, P. A.; Nagaosa, N.; Wen, X.-G. Doping a Mott Insulator: Physics of High-Temperature Superconductivity. *Rev. Mod. Phys.* **2006,** *78*, 17.
(3)   Onsager, L. A Two-Dimensional Model with an Order-Disorder Transition. *Phys. Rev.* **1944,** *65*, 117-166.
(4)   Samuelsen, E.; Silberglitt, R.; Shirane, G.; Remeika, J. Spin Waves in Ferromagnetic $CrBr_3$ Studied by Inelastic Neutron Scattering. *Phys. Rev. B* **1971,** *3*, 157.
(5)   Elmers, H.-J.; Hauschild, J.; Gradmann, U. Critical Behavior of the Uniaxial Ferromagnetic Monolayer Fe (110) on W (110). *Phys. Rev. B* **1996,** *54*, 15224.
(6)   Park, J. G. Opportunities and Challenges of 2d Magnetic Van Der Waals Materials: Magnetic Graphene? *J. Phys. Condens. Mat.* **2016,** *28*, 301001.
(7)   Cao, Y.; Fatemi, V.; Fang, S.; Watanabe, K.; Taniguchi, T.; Kaxiras, E.; Jarillo-Herrero, P. Unconventional Superconductivity in Magic-Angle Graphene Superlattices. *Nature* **2018,** *556*, 43.
(8)   Zhong, D.; Seyler, K. L.; Linpeng, X.; Cheng, R.; Sivadas, N.; Huang, B.; Schmidgall, E.; Taniguchi, T.; Watanabe, K.; McGuire, M. A. Van Der Waals Engineering of Ferromagnetic Semiconductor Heterostructures for Spin and Valleytronics. *Sci. Adv.* **2017,** *3*, e1603113.
(9)   Roldan, R.; Castellanos-Gomez, A.; Cappelluti, E.; Guinea, F. Strain Engineering in Semiconducting Two-Dimensional Crystals. *J. Phys. Condens. Mat.* **2015,** *27*, 313201.

(10)   Ghazaryan, D.; Greenaway, M. T.; Wang, Z.; Guarochico-Moreira, V. H.; Vera-Marun, I. J.; Yin, J.; Liao, Y.; Morozov, S. V.; Kristanovski, O.; Lichtenstein, A. I. Magnon-Assisted Tunnelling in Van Der Waals Heterostructures Based on $CrBr_3$. *Nat. Electron.* **2018,** *1*, 344.

(11)   Červenka, J.; Katsnelson, M.; Flipse, C. Room-Temperature Ferromagnetism in Graphite Driven by Two-Dimensional Networks of Point Defects. *Nat. Phys.* **2009,** *5*, 840.

(12)   González-Herrero, H.; Gómez-Rodríguez, J. M.; Mallet, P.; Moaied, M.; Palacios, J. J.; Salgado, C.; Ugeda, M. M.; Veuillen, J.-Y.; Yndurain, F.; Brihuega, I. Atomic-Scale Control of Graphene Magnetism by Using Hydrogen Atoms. *Science* **2016,** *352*, 437-441.

(13)   Nair, R.; Tsai, I.-L.; Sepioni, M.; Lehtinen, O.; Keinonen, J.; Krasheninnikov, A.; Neto, A. C.; Katsnelson, M.; Geim, A.; Grigorieva, I. Dual Origin of Defect Magnetism in Graphene and Its Reversible Switching by Molecular Doping. *Nat. Commun.* **2013,** *4*, 2010.

(14)   Ugeda, M. M.; Brihuega, I.; Guinea, F.; Gómez-Rodríguez, J. M. Missing Atom as a Source of Carbon Magnetism. *Phys. Rev. Lett.* **2010,** *104*, 096804.

(15)   Yazyev, O. V.; Helm, L. Defect-Induced Magnetism in Graphene. *Phys. Rev. B* **2007,** *75*, 125408.

(16)   Jung, J.; Pereg-Barnea, T.; MacDonald, A. H. Theory of Interedge Superexchange in Zigzag Edge Magnetism. *Phys. Rev. Lett.* **2009,** *102*, 227205.

(17)   Yazyev, O. V.; Katsnelson, M. Magnetic Correlations at Graphene Edges: Basis for Novel Spintronics Devices. *Phys. Rev. Lett.* **2008,** *100*, 047209.

(18)   Wang, S.; Zhang, X.; Huang, Y.; Sun, C. Q. Arsenene Nanoribbon Edge-Resolved Strong Magnetism. *Phys. Chem. Chem. Phys.* **2018,** *20*, 25716-25721.

(19)   Liu, L.; Ren, X.; Xie, J.; Cheng, B.; Liu, W.; An, T.; Qin, H.; Hu, J. Magnetic Switches Via Electric Field in BN Nanoribbons. *Appl. Surf. Sci.* **2019,** *480*, 300-307.

(20)   Liu, L.; Ren, X.; Xie, J.; Cheng, B.; Hu, J. Modulation of Magnetism Via Electric Field in MgO Nanoribbons. *arXiv1905.02328* **2019**.

(21)   Gong, C.; Li, L.; Li, Z.; Ji, H.; Stern, A.; Xia, Y.; Cao, T.; Bao, W.; Wang, C.; Wang, Y. Discovery of Intrinsic Ferromagnetism in Two-Dimensional Van Der Waals Crystals. *Nature* **2017,** *546*, 265.

(22)   Huang, B.; Clark, G.; Navarro-Moratalla, E.; Klein, D. R.; Cheng, R.; Seyler, K. L.; Zhong, D.; Schmidgall, E.; McGuire, M. A.; Cobden, D. H. Layer-Dependent Ferromagnetism in a Van Der Waals Crystal Down to the Monolayer Limit. *Nature* **2017,** *546*, 270.

(23)   Gong, C.; Zhang, X. Two-Dimensional Magnetic Crystals and Emergent Heterostructure Devices. *Science* **2019,** *363*, eaav4450.

(24)   Li, X.; Dong, B.; Sun, X.; Wang, H.; Yang, T.; Yu, G.; Han, Z. V. Perspectives on Exfoliated Two-Dimensional Spintronics. *J. Semicond.* **2019,** *40*, 081508.

(25)   Niu, J.; Yan, B.; Ji, Q.; Liu, Z.; Li, M.; Gao, P.; Zhang, Y.; Yu, D.; Wu, X. Anomalous Hall Effect and Magnetic Orderings in Nanothick V_5S_8. *Phys. Rev. B* **2017,** *96*, 075402.

(26)   Huang, B.; Clark, G.; Klein, D. R.; MacNeill, D.; Navarro-Moratalla, E.; Seyler, K. L.; Wilson, N.; McGuire, M. A.; Cobden, D. H.; Xiao, D. Electrical Control of 2D Magnetism in Bilayer CrI_3. *Nat. Nanotechnol.* **2018,** *13*, 544.

(27)   Long, G.; Zhang, T.; Cai, X.; Hu, J.; Cho, C.-w.; Xu, S.; Shen, J.; Wu, Z.; Han, T.; Lin, J. Isolation and Characterization of Few-Layer Manganese Thiophosphite. *ACS Nano* **2017,** *11*, 11330-11336.

(28)   Chu, J.; Zhang, Y.; Wen, Y.; Qiao, R.; Wu, C.; He, P.; Yin, L.; Cheng, R.; Wang, F.; Wang, Z. Sub-Millimeter-Scale Growth of One-Unit-Cell-Thick Ferrimagnetic Cr_2S_3 Nanosheets. *Nano Lett.* **2019,** *19*, 2154-2161.

(29)   Kim, K.; Lim, S. Y.; Lee, J.-U.; Lee, S.; Kim, T. Y.; Park, K.; Jeon, G. S.; Park, C.-H.; Park, J.-G.; Cheong, H. Suppression of Magnetic Ordering in Xxz-Type Antiferromagnetic Monolayer Nips 3. *Nat. Commun.* **2019,** *10*, 345.

(30)   Zhang, Y.; Chu, J.; Yin, L.; Shifa, T. A.; Cheng, Z.; Cheng, R.; Wang, F.; Wen, Y.; Zhan, X.; Wang, Z. Ultrathin Magnetic 2d Single‐Crystal Crse. *Adv. Mater.* **2019,** *31*, 1900056.

(31)   Cai, X.; Song, T.; Wilson, N. P.; Clark, G.; He, M.; Zhang, X.; Taniguchi, T.; Watanabe, K.; Yao, W.; Xiao, D. Atomically Thin CrCl3: An In-plane Layered Antiferromagnetic Insulator. *Nano Lett.* **2019**.

(32)   Wang, Z.; Zhang, T.; Ding, M.; Dong, B.; Li, Y.; Chen, M.; Li, X.; Huang, J.; Wang, H.; Zhao, X. Electric-Field Control of Magnetism in a Few-Layered Van Der Waals Ferromagnetic Semiconductor. *Nat. Nanotechnol.* **2018,** *13*, 554.

(33)   McGuire, M. A.; Dixit, H.; Cooper, V. R.; Sales, B. C. Coupling of Crystal Structure and Magnetism in the Layered, Ferromagnetic Insulator CrI3. *Chem. Mater.* **2015,** *27*, 612-620.

(34)   Kim, H. H.; Yang, B.; Li, S.; Jiang, S.; Jin, C.; Tao, Z.; Nichols, G.; Sfigakis, F.; Zhong, S.; Li, C. Evolution of Interlayer and Intralayer Magnetism in Three Atomically Thin Chromium Trihalides. *P. Natl. Acad. Sci.* **2019,** *116*, 11131-11136.

(35)   Kuo, C.-T.; Neumann, M.; Balamurugan, K.; Park, H. J.; Kang, S.; Shiu, H. W.; Kang, J. H.; Hong, B. H.; Han, M.; Noh, T. W. Exfoliation and Raman Spectroscopic Fingerprint of Few-Layer NiPS3 Van Der Waals Crystals. *Sci. Rep.* **2016,** *6*, 20904.

(36)   Freitas, D. C.; Weht, R.; Sulpice, A.; Remenyi, G.; Strobel, P.; Gay, F.; Marcus, J.; Núñez-Regueiro, M. Ferromagnetism in Layered Metastable 1T-CrTe2. *J. Phys. Condens. Mat.* **2015,** *27*, 176002.

(37)   Lee, J.-U.; Lee, S.; Ryoo, J. H.; Kang, S.; Kim, T. Y.; Kim, P.; Park, C.-H.; Park, J.-G.; Cheong, H. Ising-Type Magnetic Ordering in Atomically Thin FePS3. *Nano Lett.* **2016,** *16*, 7433-7438.

(38)   McGuire, M. A.; Clark, G.; Santosh, K.; Chance, W. M.; Jellison Jr, G. E.; Cooper, V. R.; Xu, X.; Sales, B. C. Magnetic Behavior and Spin-Lattice Coupling in Cleavable Van Der Waals Layered CrCl3 Crystals. *Phys. Rev. Mater.* **2017,** *1*, 014001.

(39)   Mermin, N. D.; Wagner, H. Absence of Ferromagnetism or Antiferromagnetism in One- or Two-Dimensional Isotropic Heisenberg Models. *Phys. Rev. Lett.* **1966,** *17*, 1133.

(40)   Bonilla, M.; Kolekar, S.; Ma, Y.; Diaz, H. C.; Kalappattil, V.; Das, R.; Eggers, T.; Gutierrez, H. R.; Phan, M. H.; Batzill, M. Strong Room-Temperature Ferromagnetism in VSe2 Monolayers on Van Der Waals Substrates. *Nat. Nanotechnol.* **2018,** *13*, 289-293.

(41)   Fumega, A. O.; Gobbi, M.; Dreher, P.; Wan, W.; González-Orellana, C.; Peña-Díaz, M.; Rogero, C.; Herrero-Martín, J.; Gargiani, P.; Ilyn, M., et al. Absence of Ferromagnetism in VSe2 Caused by Its Charge Density Wave Phase. *J. Phys. Chem. C* **2019,** *123*, 27802-27810.

(42)   Wong, P. K. J.; Zhang, W.; Bussolotti, F.; Yin, X.; Herng, T. S.; Zhang, L.; Huang, Y. L.; Vinai, G.; Krishnamurthi, S.; Bukhvalov, D. W. J. A. M. Evidence of Spin Frustration in a Vanadium Diselenide Monolayer Magnet. *Adv. Mater.* **2019,** *31*, 1901185.

(43)   O'Hara, D. J.; Zhu, T.; Trout, A. H.; Ahmed, A. S.; Luo, Y. K.; Lee, C. H.; Brenner, M. R.; Rajan, S.; Gupta, J. A.; McComb, D. W., et al. Room Temperature Intrinsic Ferromagnetism in Epitaxial Manganese Selenide Films in the Monolayer Limit. *Nano Lett.* **2018,** *18*, 3125-3131.

(44)   Kabiraj, A.; Kumar, M.; Mahapatra, S. High-Throughput Discovery of High Curie Point Two-Dimensional Ferromagnetic Materials. *npj Comput. Mater.* **2020,** *6*, 1-9.

(45)   Torelli, D.; Thygesen, K. S.; Olsen, T. High Throughput Computational Screening for 2d Ferromagnetic Materials: The Critical Role of Anisotropy and Local Correlations. *2D Mater.* **2019,** *6*, 045018.

(46)   Huang, C.; Feng, J.; Wu, F.; Ahmed, D.; Huang, B.; Xiang, H.; Deng, K.; Kan, E. Toward Intrinsic Room-Temperature Ferromagnetism in Two-Dimensional Semiconductors. *J. Am. Chem. Soc.* **2018,** *140*, 11519-11525.

(47)   Chen, S.; Wu, F.; Li, Q.; Sun, H.; Ding, J.; Huang, C.; Kan, E. Prediction of Room-Temperature Ferromagnetism in a Two-Dimensional Direct Band Gap Semiconductor. *Nanoscale* **2020,** *12*, 15670-15676.

(48)   Zheng, S.; Huang, C.; Yu, T.; Xu, M.; Zhang, S.; Xu, H.; Liu, Y.; Kan, E.; Wang, Y.; Yang, G. High-Temperature Ferromagnetism in an Fe_3P Monolayer with a Large Magnetic Anisotropy. *J. Phys. Chem. Lett.* **2019,** *10*, 2733-2738.

(49)   Huang, C.; Feng, J.; Zhou, J.; Xiang, H.; Deng, K.; Kan, E. Ultra-High-Temperature Ferromagnetism in Intrinsic Tetrahedral Semiconductors. *J. Am. Chem. Soc.* **2019,** *141*, 12413-12418.

(50)   Ataca, C.; Şahin, H.; Ciraci, S. Stable, Single-Layer MX_2 Transition-Metal Oxides and Dichalcogenides in a Honeycomb-Like Structure. *J. Phys. Chem. C* **2012,** *116*, 8983-8999.

(51)   Aras, M.; Kılıç, Ç.; Ciraci, S. Magnetic Ground State in $FeTe_2$, VS_2, and $NiTe_2$ Monolayers: Antiparallel Magnetic Moments at Chalcogen Atoms. *Phys. Rev. B* **2020,** *101*, 054429.

(52)   Chen, W.; Zhang, J.-m.; Nie, Y.-z.; Xia, Q.-l.; Guo, G.-h. Electronic Structure and Magnetism of MTe_2 (M = Ti, V, Cr, Mn, Fe, Co and Ni) Monolayers. *J. Magn. Magn. Mater.* **2020,** *508*, 166878.

(53)   Huang, C.; Deng, K.; Zhou, J.; Kan, E. Atomically Dispersed Tungsten on Metal Halide Monolayer as a Ferromagnetic Chern Insulator. *Phys. Rev. B* **2018,** *98*.

(54)   Lado, J. L.; Fernández-Rossier, J. On the Origin of Magnetic Anisotropy in Two Dimensional CrI_3. *2D Mater.* **2017,** *4*, 035002.

(55)   Perdew, J. P.; Burke, K.; Ernzerhof, M. Generalized Gradient Approximation Made Simple. *Phys. Rev. Lett.* **1996,** *77*, 3865.

(56)   Monkhorst, H. J.; Pack, J. D. Special Points for Brillouin-Zone Integrations. *Phys. Rev. B* **1976,** *13*, 5188-5192.

(57)   Heyd, J.; Scuseria, G. E.; Ernzerhof, M. Hybrid Functionals Based on a Screened Coulomb Potential. *J. Chem. Phys.* **2003,** *118*, 8207.

(58)   Anisimov, V. I.; Zaanen, J.; Andersen, O. K. Band Theory and Mott Insulators: Hubbard U Instead of Stoner I. *Phys. Rev. B* **1991,** *44*, 943-954.

(59)   Kan, M.; Adhikari, S.; Sun, Q. Ferromagnetism in MnX_2 (X= S, Se) Monolayers. *Phys. Chem. Chem. Phys.* **2014,** *16*, 4990-4994.

(60)   Kan, M.; Zhou, J.; Sun, Q.; Kawazoe, Y.; Jena, P. The Intrinsic Ferromagnetism in a MnO_2 Monolayer. *J. Phys. Chem. Lett.* **2013,** *4*, 3382-3386.

(61)   Lan, M.; Xiang, G.; Nie, Y.; Yang, D.; Zhang, X. The Static and Dynamic Magnetic Properties of Monolayer Iron Dioxide and Iron Dichalcogenides. *RSC Adv.* **2016,** *6*, 31758-31761.

(62)   Liu, L.; Zhang, X. A User Friendly and Efficient Tool Implementing Monte Carlo Simulations to Estimate Curie/Neel Temperature. https://github.com/golddoushi/mcsolver.